Spectrometer for hard X-ray free-electron laser based on diffraction focusing

V. G. Kohn,[a] O. Y. Gorobtsov[b] and I. A. Vartanyants[b,c]*

[a]National Research Center 'Kurchatov Institute', Kurchatov Square 1, 123182 Moscow, Russia, [b]Deutsches Electronen-Synchrotron DESY, Notkestrasse 85, D-22607 Hamburg, Germany, and [c]National Research Nuclear University, 'MEPhI', 115409 Moscow, Russia.
E-mail: ivan.vartaniants@desy.de

X-ray free-electron lasers (XFELs) generate sequences of ultra-short spatially coherent pulses of X-ray radiation. A diffraction focusing spectrometer (DFS), which is able to measure the whole energy spectrum of the radiation of a single XFEL pulse with an energy resolution of $\Delta E/E \simeq 2 \times 10^{-6}$, is proposed. This is much better than for most modern X-ray spectrometers. Such resolution allows one to resolve the fine spectral structure of the XFEL pulse. The effect of diffraction focusing occurs in a single-crystal plate due to dynamical scattering, and is similar to focusing in a Pendry lens made from a metamaterial with a negative refraction index. Such a spectrometer is easier to operate than those based on bent crystals. It is shown that the DFS can be used in a wide energy range from 5 keV to 20 keV.

1. Introduction

Hard X-ray free-electron lasers (XFELs) (Emma et al., 2010; Ishikawa et al., 2012; Altarelli et al., 2006) generate sequences of ultra-short spatially coherent pulses of X-ray radiation. These pulses can be less than 100 fs in duration, and have an energy spectrum of relative width $\Delta\omega/\omega \simeq 10^{-3}$ (see, for example, Altarelli et al., 2006). Such characteristics make XFELs useful for a wide range of applications, including potentially three-dimensional imaging of individual macromolecules, looking at dynamics of chemical reactions, and many others. It is well known that the XFEL pulse energy spectrum has a fine structure, which changes chaotically from pulse to pulse. This fine structure has a characteristic width of the order of $\Delta\omega/\omega \simeq 10^{-6}$ for hard X-ray energies. Therefore, it is of interest to elaborate a spectrometer with sufficient resolution to resolve these fine features for each pulse individually.

Since each pulse of the XFEL has a unique structure in the energy spectrum, the spectrometer has to be able to detect the whole spectrum of a single pulse simultaneously. Obviously, the scan of the energy region by the monochromator, as it is conventionally performed at synchrotron sources, cannot be applied at XFELs. Most of the known spectrometers (for example, Kleimenov et al., 2009; Dickinson et al., 2008) of such type have a maximum energy resolution of 10^{-5}. They are based on the Bragg diffraction of curved or flat single crystals, and their resolution is limited by the angular divergence of the reflected beam due to dynamical scattering effects. Recently, a

few spectrometers (Zhu et al., 2012; Inubushi et al., 2012) were proposed and tested at XFEL sources. The first one was based on a curved crystal in the Bragg scattering geometry and has a resolving power of 2.4×10^{-5}. The second one uses an elliptical mirror and silicon crystal as an analyzer and showed a resolution of 2×10^{-6} at 1 Å wavelength.

We propose a new spectrometer based on the effect of single-crystal diffraction focusing (Afanas'ev & Kohn, 1977). A sketch of the diffraction focusing spectrometer (DFS) is shown in Fig. 1. In this spectrometer the incoming divergent beam from a secondary source is focused by a single-crystal plate at each energy near the Bragg angle. Since the Bragg angle depends on the energy, X-rays with different energies
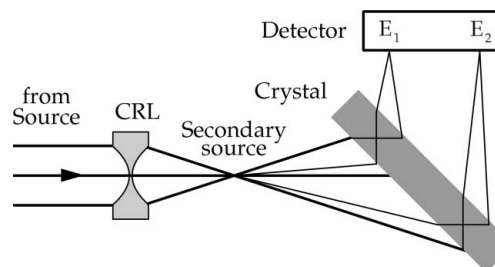
Figure 1
Schematic view of the beamline with the diffraction focusing spectrometer. The incoming beam from the source is focused by the compound refractive lenses (CRLs) and creates the secondary source. The flat crystal is positioned in a Laue geometry behind this secondary source. The high-resolution detector is located close to the crystal in the direction of the diffracted beam.

will be focused at different points just behind the crystal under conditions of focusing. Due to this property a higher-resolution spectrometer can be developed.

In order to achieve high resolution, the effective size of the secondary source should be decreased to about a few micrometers and the angular divergence of the beam increased to the necessary value. This can be done, for example, by positioning compound refractive lenses (CRLs) (Snigirev *et al.*, 1996, 1998) upstream from the DFS. Planar silicon CRLs allow one to achieve a small focusing distance (a few centimeters), and to obtain a source image of small size even at high photon energies.

The effect of single-crystal diffraction focusing was first predicted by Afanas'ev & Kohn (1977) and considered in detail by Kohn (1979). It was experimentally confirmed by Aristov *et al.* (1978, 1980, 1982) and by Koz'mik & Mikhailyuk (1978). Recently the effect of focusing in bent-crystal systems was considered theoretically by Mocella *et al.* (2004, 2008) and by Nesterets & Wilkins (2008) as a way for improving polychromatic focusing.

The effect of diffraction focusing is similar to one predicted in metamaterials with a negative refractive index for long-wavelength radiation. For these materials, Pendry (2000) has introduced a lens in the form of a plane slab made from the metamaterial. The divergent incident beam is focused first inside the slab and then behind it.

For X-rays an effective negative refraction occurs for a wave for which, owing to dynamical diffraction in the Laue case, the Pointing vector has an opposite direction to the angular deviation of the incident wave from the Bragg angle. As a result, a slightly divergent beam incident at the Bragg angle at the single crystal is focused first inside the crystal and then once again behind the crystal. The difference from the Pendry lens is that the angular width of the focused beam is equal to the angular range of the dynamical diffraction (tens of microradians), and is rather small. Nevertheless, this effect allows one to obtain a beam of a few micrometers width. The width of the focused beam determines the resolution of the DFS. In this work we investigate the optimal conditions for such a spectrometer based on diffraction focusing and show that the energy resolution of the DFS can reach 10^{-6}. Such resolution will be sufficient to resolve the fine structure of the hard X-ray FEL pulse spectrum.

2. Theory and analytical estimates of the achievable resolution

Our goal is to obtain an estimate of the resolution of the spectrometer based on diffraction focusing. To obtain this value it is necessary to calculate the full width at half-maximum (FWHM) of the intensity profile of the focused monochromatic beam at the detector position. The main components of the DFS are shown in Fig. 2. The crystal, in the form of plane parallel plate of thickness t, is located at a distance L_0 from the point source located at the coordinate x_s in the plane of the secondary source formed by the CRL (Fig. 1). The detector plane is positioned at a distance L_1 and
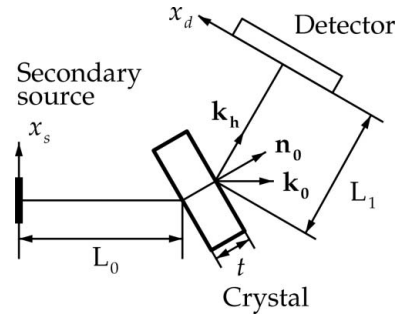

Figure 2
Main components of the diffraction focusing spectrometer. The secondary source plane is described by the coordinate x_s, the crystal is positioned at a distance L_0 from the source, and the detector is located at a distance L_1 from the crystal in the direction of the Laue diffracted beam defined by the vector $\mathbf{k}_h$. The detector plane is described by the coordinate x_d.

is perpendicular to the direction of the diffracted beam with the wavevector $\mathbf{k}_h$. The coordinate x_d is related to the point of observation at the detector. The angles φ_0 and φ_h between the normal to the crystal surface 0 and the wavevectors $\mathbf{k}_0$, $\mathbf{k}_h$ determine the asymmetry of the diffraction; their sum is equal to $2\theta_B$, where θ_B is the Bragg angle.

The amplitude of the diffracted wave $E_h(x_d)$ at the detector position in the scheme shown in Fig. 2 was obtained by Afanas'ev & Kohn (1971). It was derived by introducing the crystal propagator in the form of the Green function for the Takagi equations (Authier, 2005), and the Kirchhoff propagator, describing the transmission in free space in paraxial approximation. In the following paper by Kohn *et al.* (2000) the final form of this amplitude was obtained by using Fourier transform in reciprocal space. Using this approach the amplitude of the diffracted wave $E_h(x_d)$ can be presented in the following way

$$E_h(x_d) = C_1 \int_{-\infty}^{\infty} \frac{d\eta}{S(\eta)} \sum_{\pm} \{\pm \exp[\Phi_{\pm}(\eta) - M_{\pm}(\eta)]\}. \quad (1)$$

Here the positive sign corresponds to the weakly absorbed wave, and the negative sign to the strongly absorbed wave,

$$\Phi_{\pm}(\eta) = \frac{\pi\alpha}{\Lambda}\left(x_d - x_C - \frac{x_s}{\beta}\right)\eta - \frac{\pi t_0}{2\Lambda}\eta^2 + \Phi_{\pm}^{(0)}(\eta),$$

$$\Phi_{\pm}^{(0)}(\eta) = \pm\frac{\pi t}{\Lambda}S(\eta), \quad S(\eta) = (1 + \eta^2)^{1/2},$$

$$M_{\pm}(\eta) = \frac{\mu_0 t}{2(\gamma_0\gamma_h)^{1/2}}\left[\frac{(\beta+1)}{2\beta^{1/2}} \mp \frac{\varepsilon_h}{S(\eta)} \mp \frac{\eta}{S(\eta)}\frac{(\beta-1)}{2\beta^{1/2}}\right], \quad (2)$$

$$C_1 = \frac{(\lambda L_t)^{1/2}}{2 S_B \Lambda \beta^{1/2}}, \quad \mu_0 = K\chi_{i0}, \quad K = 2\pi/\lambda.$$

In these equations the following parameters are used: λ is the wavelength in a vacuum, μ_0 is the linear absorption coefficient, $L_t = L_0 + L_1$, $S_B = \sin(2\theta_B)$,

research papers

$$\Lambda = \frac{\lambda(\gamma_0\gamma_h)^{1/2}}{|\chi_{rh}|}, \quad t_0 = \frac{2|\chi_{rh}|\gamma_0^{3/2}}{S_B^2\gamma_h^{1/2}}\widetilde{L}, \quad \widetilde{L} = \frac{L_0}{\beta^2} + L_1,$$

$$x_C = x_0 - x_L, \quad x_L = \lambda\widetilde{L}q_0/2\pi, \quad x_0 = \frac{1}{2}t\gamma_h(T_h - T_0),$$

$$q_0 = \frac{K|\chi_{r0}|}{2S_B}(\beta - 1), \quad \varepsilon_h = \chi_{ih}/\chi_{i0}, \quad \alpha = 2\gamma_0/S_B,$$

$$T_{0,h} = \tan(\varphi_{0,h}), \quad \gamma_{0,h} = \cos(\varphi_{0,h}), \quad \beta = \gamma_0/\gamma_h.$$

$$(3)$$

In equations (2) and (3) Λ is the extinction length, t_0 is an effective focusing thickness of the crystal, $\widetilde{L}$ is the effective distance from the source to the detector, x_0 and x_L are the displacements of the image due to asymmetry of the diffraction geometry, and $\chi_{0,h} = \chi_{r0,h} + i\chi_{i0,h}$ are the Fourier components of the complex susceptibility of the crystal for the angles of scattering 0 and $2\theta_B$. The intensity distribution at the detector position x_d for a point source at the position x_s is given by the square modulus of the amplitude $E_h(x_d)$ [equation (1)], $I_h(x_d) = |E_h(x_d)|^2$. For a geometrical optics description of the effect of diffraction focusing, see Appendix A.

The DFS energy resolution is determined by the condition that a shift of the photon energy ΔE leads to a shift of the diffracted beam center by $x_{d\omega}$ at the detector plane. It was shown by Kohn *et al.* (2000) that

$$x_{d\omega} = \left(\frac{L_0}{\beta} - L_1\right)\tan\theta_B\frac{\Delta E}{E}. \tag{4}$$

We will consider now the case of the crystal thickness $t = t_0$ when focusing conditions are satisfied at the detector position. To obtain an estimate of the DFS resolution the shift of the beam position $x_{d\omega}$ in equation (4) has to be compared with the beam size (FWHM) Δ_x at the detector position. To obtain an analytical estimate of the beam size we will consider two cases of weakly absorbing ($\mu_0t_0 \ll 1$) and strongly absorbing ($\mu_0t_0 \gg 1$) crystals.

In the first case we can neglect absorption and consider in equation (1) the central part of the integration region with $\eta \ll 1$. This approximation is justified if the additional condition $\Lambda \ll t_0$ is satisfied as well. In equation (1) we can consider only one term with the positive sign, as the other term with the negative sign corresponds to defocusing conditions. Expanding $S(\eta)$ in the Taylor series up to the fourth order in η one can obtain

$$E_h(x_d) \simeq C_1 \int_{-\infty}^{\infty} d\eta \exp\left[i\pi\eta s + i\frac{\pi(t-t_0)}{\Lambda}\frac{\eta^2}{2} - i\frac{\pi t}{\Lambda}\frac{\eta^4}{8}\right], \tag{5}$$

where

$$s = \frac{\alpha}{\Lambda}\left(x_d - x_C - \frac{x_s}{\beta}\right) \tag{6}$$

is the dimensionless coordinate at the detector position. As soon as we consider small values of η, the integral in (5) reaches its maximum value if the conditions $t = t_0$ and $s = 0$ are satisfied simultaneously. In fact, the first condition is the condition of focusing. It also defines the focusing crystal

thickness t_0, that, according to its definition in equation (3), is proportional to the effective distance from the source to the detector $\widetilde{L}$. This effective distance is equal to the total distance L_t in the symmetrical ($\beta = 1$) scattering geometry.

The integral in equation (5) is similar to the one describing the diffraction by a parabolic mirror (Berry & Klein, 1996). Therefore, the diffraction pattern in the case of small absorption, when the phase term plays the main role, is similar to the one resulting from the parabolic mirror focusing.

To obtain an estimate of the focused beam size, we note that the exponential in the integrand becomes a fast oscillating function for small values of s outside the region where the term η^4 is less than π. Therefore, we can exclude this region from the integration, and consider the integral in the finite limits from $-\eta_0$ to η_0, where

$$\eta_0 \simeq (8\Lambda/t_0)^{1/4}. \tag{7}$$

Then we have for the amplitude in equation (5),

$$\frac{E_h(x_d)}{C_1} \simeq \int_{-\eta_0}^{\eta_0} d\eta \exp(i\pi\eta s) = 2\eta_0\frac{\sin(\pi\eta_0 s)}{\pi\eta_0 s}. \tag{8}$$

Thus, we arrive at the conclusion that the amplitude of the focused wave in a weak absorption case is described by a sinc function, for which the size (FWHM) of the intensity distribution is given by

$$\Delta_{xp} = 0.83\frac{\Lambda^{3/4}t_0^{1/4}}{\pi\alpha}. \tag{9}$$

The second case of strong absorption was discussed earlier by Afanas'ev & Kohn (1977). Again, in equation (1) we take into consideration only one term with the positive sign for which the Borrmann effect takes place in the region of small $\eta \ll 1$. In this case the absorption term cannot be neglected, and we can expand functions $\Phi_+(\eta)$ and $M_+(\eta)$ in the exponent of the Taylor series up to the second order in η and obtain for the amplitude

$$E_h(x_d) \simeq C_2 \int_{-\infty}^{\infty} d\eta \exp(i\pi s\eta - \sigma_1\eta^2 + \sigma_2\eta), \tag{10}$$

where

$$C_2 = C_1 \exp\left\{-\frac{\mu_0t_0}{2(\gamma_0\gamma_h)^{1/2}}\left[\frac{(\beta+1)}{2\beta^{1/2}} - \varepsilon_h\right]\right\},$$
$$\sigma_1 = \frac{\mu_0t_0\varepsilon_h}{4(\gamma_0\gamma_h)^{1/2}}, \quad \sigma_2 = \frac{(\beta-1)\mu_0t_0}{4\gamma_0}. \tag{11}$$

The integral (10) is similar to the well known Fourier transform of the Kirchhoff propagator,

$$\int_{-\infty}^{\infty} \frac{dq}{2\pi}\exp\left(iqx - i\frac{\lambda z}{4\pi}q^2\right) = \frac{1}{(i\lambda z)^{1/2}}\exp\left(i\pi\frac{x^2}{\lambda z}\right), \tag{12}$$

and can be calculated analytically as

$$E_h(x_d) \simeq C_3 \exp\left(i2\pi\sigma_2 s - \frac{\pi^2}{4\sigma_1}s^2\right), \qquad (13)$$
$$C_3 = C_2(\pi/\sigma_1)^{1/2}\exp\left(-\sigma_2^2/4\sigma_1\right).$$

Now the size (FWHM) of the intensity distribution in the focus for a strong absorption case is equal to

$$\Delta_{xa} = (2\ln 2)^{1/2}\frac{\Lambda}{\pi\alpha}\sigma_1^{1/2}. \qquad (14)$$

Direct computer simulations show that both values of the peak size Δ_{xp} and Δ_{xa}, defined by the equations (9) and (14), give an excellent estimate within the region of their validity. However, in some intermediate cases the region of integration is limited by the phase but absorption cannot be neglected inside this region. In these cases there is no analytical solution for the amplitude of the diffracted wave and for the estimate of the beam size one should calculate the following integral numerically,

$$E_h(x_d) = C_2 \int_{-\eta_0}^{\eta_0} d\eta \exp\left(i\pi s\eta - \sigma_1\eta^2 + \sigma_2\eta\right), \qquad (15)$$

and then estimate Δ_x as the FWHM of the intensity curve.

Finally, the energy resolution of the DFS can be obtained using the Rayleigh criterion (Born & Wolf, 2000), i.e. two peaks are resolved if the intermediate point between them has a height less than 80% of the maximum height. Taking into account equation (4) we obtain for the energy resolution

$$\frac{\Delta E}{E} = \frac{1.15\beta\Delta_x}{(L_0 - L_1\beta)\tan\theta_B}. \qquad (16)$$

To increase the resolution one has to consider L_0 to be as large as possible and L_1 as small as possible. Analytical results obtained for the beam size Δ_x [equations (9) and (14)] allow one to estimate the influence of the asymmetry factor β.

In the case of low absorption, substituting equation (3) into (9) and considering the distance $L_1 = 0$ we obtain for the beam size (FWHM),

$$\Delta_{xp} = \frac{0.83}{2\pi}\frac{\lambda^{3/4}S_B^{1/2}(2L_0)^{1/4}}{|\chi_{rh}|^{1/2}\beta^{3/4}}. \qquad (17)$$

Substituting this equation into the expression (16) we find that the resolution can be, in principle, increased in the asymmetric case with $\beta \ll 1$. Unfortunately, the gain is very small since $\Delta E/E \propto \beta^{1/4}$. It is also known that small values of β are difficult to realise in practice because the surface of the crystal must be cut at a definite angle with the reflecting atomic planes close to the Bragg angle, which also depends on the radiation energy. On the other hand, as follows from equations (2), for small values of β the source of size S will increase the size of the focused beam to the value S/β. This will reduce the effective resolving power of the DFS. In the following, we will perform computer simulations and present results only for the symmetrical ($\beta = 1$) scattering geometry.

3. Results and discussion

In practical applications of diffraction focusing one should have single crystals of the highest quality such as Si and Ge. Taking into account the high power of the XFEL pulses and the demand of high thermal conductivity, a single perfect diamond crystal, below referenced as C, can also be an attractive choice for the XFEL spectrometer. These three materials were considered in our simulations. The 220 and 400 reflections were analyzed in our work for which a strong Borrmann effect (Authier, 2005) takes place. Detailed computer simulations were performed for the photon energy $E = 12.4$ keV ($\lambda = 1$ Å). At this photon energy the absorption coefficients are: $\mu_0 = 39.8$ cm^{-1} for Si, $\mu_0 = 810.0$ cm^{-1} for Ge and $\mu_0 = 3.15$ cm^{-1} for C. We note that at this photon energy, and with crystal thicknesses defined by the parameter t_0 in equation (3), Si and diamond crystals can be considered as thin crystals, whereas the Ge crystal is of an intermediate thickness.

It follows from (16) that for a best DFS resolution the distance L_0 should be as large as possible while the distance L_1, on the contrary, should be as small as possible. In our simulations we considered the following distances: $L_0 = 10$ m and $L_1 = 0.1$ m. Our simulations show that small variations of these values do not significantly influence results.

The intensity distribution at the position of the detector as a function of crystal thickness t for a Laue diffracted beam, Si 220 reflection and point source is presented in Fig. 3. The two-dimensional intensity distribution in the plane of parameters (x_d, t) is presented in Fig. 3(a) and a cut through this distribution at the center of the detector position $x_d = 0$ in Fig. 3(b). Intensity values are normalized to the values at the same position along the optical axis but without a crystal. It is seen in this figure that at the crystal thickness $t = t_0 = 360$ µm the incoming X-ray beam is focused on the exit surface of the crystal. The relative intensity is also increased to about three times compared with a beam without a crystal. What can also be seen in Fig. 3(a) are oscillations of intensity as a function of
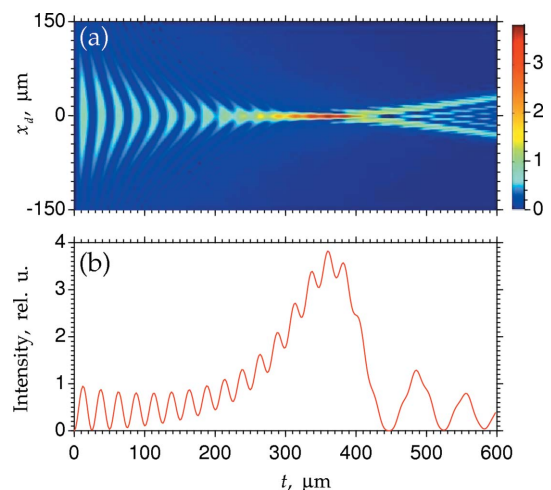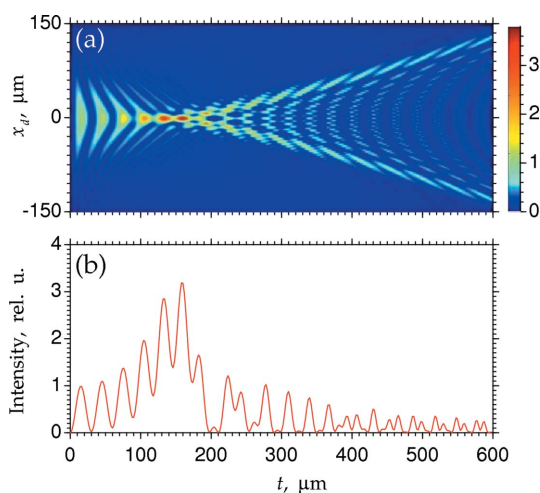

Figure 3
The case of a silicon 220 reflection. (a) Two-dimensional distribution of the intensity. (b) Intensity in the central position of the image $x_d = 0$ as a function of crystal thickness t.

crystal thickness. They have been observed before in experiments on wedge-shaped crystals (Aristov *et al.*, 1978, 1980). For small thicknesses $t \leq t_0$, when absorption can be neglected, these oscillations are due to strong interference between two types of Bloch waves [corresponding to the two signs in equation (1)] inside a crystal. The form of these oscillations is different from those observed with a point source at the entrance surface of the crystal and described by Kato (1961); this is why it is called the anomalous Pendellösung effect.

The period of oscillations at $x_d = 0$ (see Fig. 3a) is equal to the extinction length Λ [see equation (3)]. In our scattering conditions $\Lambda = 25.1$ µm. On the other hand, the thickness of diffraction focusing $t_0 = 360$ µm, so the condition $\Lambda \ll t_0$ is easily satisfied. With increasing crystal thickness the weakly absorbed field becomes larger due to focusing effects, whereas the strongly absorbed field becomes smaller due to both defocusing and absorption effects. However, for the focusing crystal thickness the interference between two fields still exists, and leads to oscillations of the peak intensity. For the conditions of optimal resolution, a crystal thickness in the focal region should be considered that provides the minimum beam size.

Our analysis showed that a diamond crystal can be considered as a good candidate for a DFS. The results of computer simulation for the diamond crystal and 220 reflection are presented in Fig. 4. In this case the crystal thickness at which focusing occurs, $t_0 = 158$ µm, is smaller than that in a Si crystal, while the extinction length is slightly larger, $\Lambda = 30$ µm. The absorption is also smaller for a diamond crystal. As a result, strong interference fringes do not vanish at the crystal thickness corresponding to the focusing conditions. It is interesting that in this case, for the large crystal thicknesses, well pronounced Kato oscillations can be observed. They have the opposite sign of curvature compared with the anomalous Pendellösung fringes discussed before. One can call fringes at small crystal thicknesses plane-wave interference, and fringes at the large crystal thicknesses spherical-wave interference.
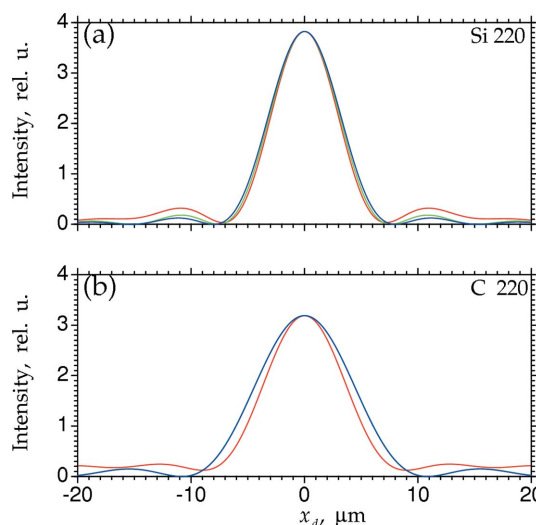
The latter occurs at crystal thicknesses just behind the crystal thickness t_0 corresponding to the focusing conditions, where the focus itself can be considered as a secondary source. It is similar to the case considered by Kato (1961) with the source at the entrance surface of the crystal, if we separate the crystal into two parts. The first part creates the secondary source and the second part gives the spherical-wave interference.

We also performed simulations for Si 400 and diamond 400 reflections and obtained the crystal thicknesses t_0 corresponding to focusing conditions, *i.e.* 182 µm and 80 µm, respectively. However, in these cases we obtained even stronger interference effects. For practical reasons it is better to use crystals and reflections where these interference effects are minimized, due to the fact that oscillations of intensity in the focal region smear the focal point and make application of these crystals and reflections for the DFS more problematic. We also considered the cases of Ge 220 and Ge 400 reflections where absorption is much stronger than in Si and diamond crystals, and interference fringes are not observed. Unfortunately, the intensity of the Laue diffracted beam is also strongly suppressed for Ge crystals at these reflections making Ge crystals inappropriate for DFS applications. Finally, our analysis has shown that for DFS applications the most prominent candidates are Si 220 and diamond 220 reflections.

As follows from our simulations [see Figs. 3(a) and 4(a)] the size of the beam in the focal position is of the order of a few micrometers. The beam profile in the focal position (at crystal thickness $t = t_0$) for two cases of Si and diamond crystals (220 reflection) is shown in Fig. 5. In this figure results of computer simulations are presented together with the results of analytical estimates obtained in the previous section. In the case of

Figure 4
The case of a diamond 220 reflection. (*a*) Two-dimensional intensity distribution. (*b*) Intensity in the central position at $x_d = 0$ as a function of crystal thickness *t*.

Figure 5
Comparison of the intensity profiles at the detector position. (*a*) Silicon 220 reflection, crystal thickness $t_0 = 360$ µm. Direct calculations using equation (1) (red line) and analytical results based on equations (8) (blue line) and (15) (green line) are presented. (*b*) Diamond 220 reflection, crystal thickness $t_0 = 158$ µm. Direct calculation using equation (1) (red line) and analytical results based on equations (8) and (15) (blue line) are presented. Both intensity profiles obtained from the analytical result completely coincide with each other in this case.
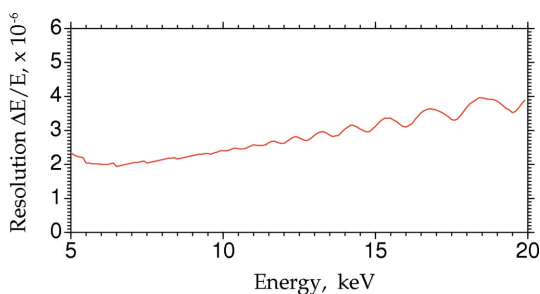
Table 1
Size (FWHM) of the beam in the focal position (µm).

	Si 220	Si 400	C 220	C 400
Equation (1)	6.6	7.9	8.2	10.7
Equation (8)	6.7	8.9	9.6	12.7
Equation (15)	7.1	9.3	9.7	12.8

Table 2
Energy resolution of the DFS at 12.4 keV ($\times 10^6$).

Reflection	Si	C
220	3.1	2.5
400	2.7	2.0

a Si crystal (Fig. 5a), analytical results obtained using equations (8) and (15) are slightly different but give an excellent estimate of the beam shape in the focus compared with the curves obtained from the computer simulations. In the case of a diamond crystal (see Fig. 5b), both analytical curves completely coincide with each other in the focal region. This is not surprising as both estimates should give good results for a low absorption, which is the case for the diamond crystal. The approximate curve is close to the one calculated according to the expression (1); however, it has a slightly larger width. In Table 1 the size of the beam (FWHM) in the focal position for a crystal thickness $t = t_0$, obtained from computer simulations, in the case of Si and diamond crystals is presented. As follows from our simulations, typical beam sizes are of the order of a few micrometers, which means that the detector should have a resolution of the order of 1 µm, or better.

The energy resolution of the spectrometer for a photon energy of 12.4 keV, reflections 220 and 400 for Si and diamond crystals was estimated using equation (16) and is summarized in Table 2. Our results show that at this energy the resolution of the DFS is within the range $(2–3) \times 10^{-6}$. As follows from our simulations, the highest resolution is achieved with the diamond crystals and 400 reflection. It is interesting to investigate the energy resolution as a function of energy at a fixed crystal thickness. Results of our simulations for the energy range 5–20 keV, Si crystal, 220 reflection and crystal thickness $t = 360$ µm are presented in Fig. 6. As can be seen from this figure, at lower energies, about 6 keV, the resolution is even higher than that at the photon energy 12.4 keV. At higher energies the resolution decreases with energy and starts to oscillate. However, up to an energy of 20 keV it stays below the value 5×10^{-6} that is sufficient for the effective use of the DFS. The presence of oscillations in the energy dependence of the resolution can be understood considering the fact that the focusing crystal thickness t_0 is energy dependent. As a result,

interference between two fields (strongly and weakly absorbed) in the crystal can be observed in the energy range as well.

4. Applications of DFS at XFEL

Here we will discuss in more detail whether the resolution of the DFS described in the previous sections is sufficient to resolve the fine structure of individual XFEL pulses. To answer this question we simulate the spectral distribution of the incoming XFEL pulse and analyze its shape after Laue diffraction from the crystal. To simulate the initial XFEL energy spectrum we used an approach proposed by Pfeifer et al. (2010) where a double Fourier transform in the spectral and time domains is used starting with the spectrum containing 'white' noise in the phase. The initial XFEL pulse generated according to this procedure is shown in Fig. 7(a). We assumed here an incoming photon energy of 12.4 keV, pulse duration $T = 100$ fs and spectral width $\Delta\omega/\omega = 10^{-3}$. As can be seen from this figure, the generated pulse spectrum has the typical behavior of a SASE (self-amplified spontaneous emission) XFEL pulse (see, for example, Altarelli et al., 2006). The spectrum of this pulse obtained after a Laue 220 diffraction from a Si crystal is presented in Fig. 7(b). In our simulations we considered the experimental geometry shown in Fig. 2 with

Figure 6
Resolution of the DFS as a function of the photon energy for the case of the Si 220 reflection. Simulations were performed for crystal thickness $t = 360$ µm.

Figure 7
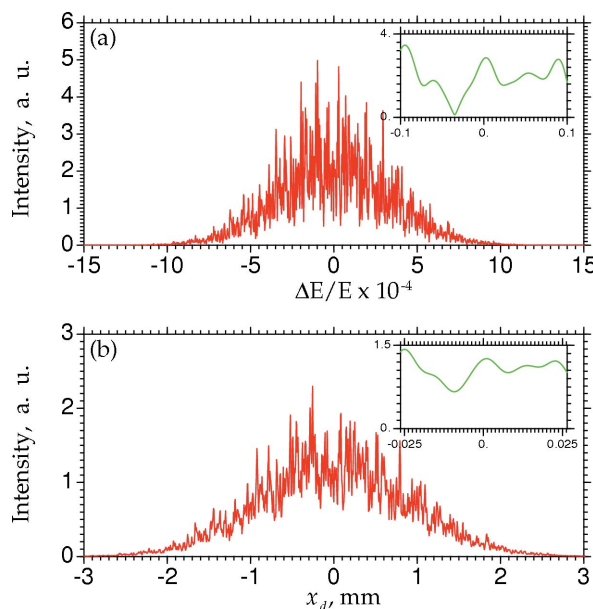(a) Simulated XFEL spectrum with an incoming photon energy of 12.4 keV, pulse duration $T = 100$ fs and spectral width $\Delta\omega/\omega = 10^{-3}$. (b) Corresponding intensity distribution at the detector after 220 diffraction of this pulse from a Si crystal. Insets show an enlarged part of the spectrum.

distances $L_0 = 10$ m and $L_1 = 0.1$ m. It can be seen in Fig. 7 that all main features of the energy spectrum of the incoming XFEL pulse are well resolved and reproduced at the detector. However, owing to the finite resolution of the DFS, a small additional background can be observed in Fig. 7(b) as well.

In the simulations presented in Fig. 7, a point source and a wide angular divergence of the incident beam were assumed. In principle, the finite source size could reduce the energy resolution of the DFS. As follows from equation (2), in order to keep the resolution value of the DFS on the same level, the source size should be significantly smaller then the beam size in the focal position. According to our results obtained in the previous section, a source size of the order of, or smaller than, 1 µm will be sufficient to keep the resolution on the level of 10^{-6}. Since at XFELs the source sizes are of the order of a few tens of micrometers (Altarelli et al., 2006), the focusing optics is an important element for effective use of the DFS.

Another important point for an effective use of the DFS at XFELs is the possibility of measuring the whole energy spectrum of a single pulse. Two conditions should be satisfied in order to reach this goal. The first one puts limitations on the angular divergence θ of the incoming beam. Taking into account that the divergence of the incoming beam should be larger than the acceptance angle defined by the Bragg condition, we obtain $\theta > \tan\theta_B(\Delta\omega/\omega)$. For a typical bandwidth of XFEL sources, $\Delta\omega/\omega \simeq 10^{-3}$ and reflections considered in our simulations with $\tan\theta_B \simeq 0.3/0.7$, we obtain the following condition for a minimum divergence, $\theta_0 > 7 \times 10^{-4}$. This condition can be well satisfied by using CRLs. Chromatic aberrations that are an intrinsic property of CRLs can be neglected for DFS applications because the relative interval $\Delta E/E$ is rather small, about 10^{-3} (see, for details, Kohn, 2012). The angular aperture θ_l of the parabolic absorbing lens is equal to $\theta_l = \delta(\lambda/R\beta)^{1/2}$, where the complex index of refraction is assumed as $n = 1 - \delta + i\beta$, and R is the curvature radius at the apex of the parabola. For a Si lens and $\lambda = 1$ Å, absorption and refraction indices are equal to $\delta = 3.2 \times 10^{-6}$ and $\beta = 3.2 \times 10^{-8}$. Therefore, from the inequality $\theta_l > \theta$, we arrive at the condition $R < 0.8$ µm, which is easy to satisfy in practice.

The second condition follows from the size of the spectrum Δx_d at the detector position. Clearly, the detector window as well as the crystal longitudinal size have to be larger than the spectrum size Δx_d. It follows from equation (4) that $\Delta x_d > L_0\theta_0 = 7$ mm for $L_0 = 10$ m and $\theta_0 = 7 \times 10^{-4}$. For a pixel size of 5 µm the detector has to have more than 1400 pixels that can be afforded by present detectors.

5. Summary

In summary, we propose a spectrometer for XFELs based on the effect of diffraction focusing, that theoretically allows an energy resolution of $\Delta E/E \simeq 2 \times 10^{-6}$ to be achieved. This is better than in most existing spectrometers, and should allow, in principle, the fine structure of individual XFEL pulses to be resolved. We investigated different crystals and possible reflections and came to the conclusion that the favorable ones are silicon and diamond single crystals with the 220 reflection. We obtained analytical solutions for the spectrometer resolution in two limits of strongly and weakly absorbing crystals and compared them with computer simulations. In order to measure the full spectrum the incoming beam should have sufficient divergence that can be obtained, for example, by focusing of the incoming beam with CRLs. The proposed spectrometer is easy to operate and can be installed at any hard X-ray beamline at an XFEL. By analyzing the resolving power of the DFS we determined that the detector resolution should be of the order of 1 µm, or below what can be achieved by present detectors. Finally, we foresee that a spectrometer based on diffraction focusing will be widely used for the spectral analysis of individual pulses of the present and future hard X-ray FELs.

APPENDIX A
Geometrical optics approach for description of diffraction focusing

Here, we will describe a process of diffraction focusing on the basis of the geometrical optics approximation (see Fig. 8). In geometrical optics the ray trajectories from the source to the detector are considered. First, the base trajectory, which is used in the derivation of equation (1) has to be defined. This trajectory starts from the source and goes to the crystal at the Bragg angle with the diffracting atomic planes, after taking into account the refraction at the crystal surface. Inside the crystal it travels along the atomic planes in the symmetrical case of diffraction. Behind the crystal it travels along the direction of the reflected beam. This trajectory is shown in Fig. 8 by the red line. It defines the origin on the detector coordinate x_d axis, i.e. it corresponds to the point $x_d = 0$. The integration variable η in equation (1) is proportional to the angular deviation from this base trajectory. Each value of η corresponds to the ray, and all rays make a total contribution to the detector image. As usual, the trajectory of the ray is defined from the calculation of the integral (1) by means of the stationary phase method.
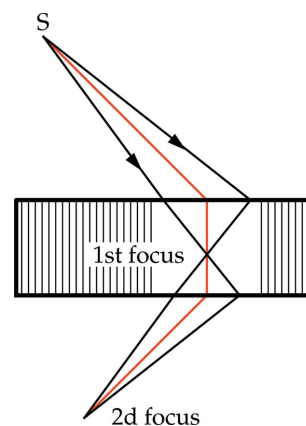
Figure 8
Schematic view of diffraction focusing based on a geometrical optics approach.

The main contribution to the integral corresponds to the region where the condition

$$\frac{d\Phi_{\pm}(\eta)}{d\eta} = 0 \qquad (18)$$

is satisfied. We are interested in the small values of $\eta \ll 1$. Therefore, we can consider only the linear term in the Taylor series over η. In addition, we restrict ourselves by the symmetrical case $\beta = 1$.

Let us consider first the case in front of the crystal. Then $L_1 = t = 0$ and from equations (18), (2) and (3) we have

$$x_d = \frac{|\chi_{rh}|}{S_B} L_0 \eta. \qquad (19)$$

As follows from (19), the coordinate x_d is proportional to the angular deviation parameter η. This is the usual situation for a spherical wave. Let us consider, in addition, the crystal plate of definite thickness t. Now we obtain two trajectories according to the two signs in the equation. They belong to two branches of the dispersion surface which are well known in the theory of plane-wave diffraction in crystals (Authier, 2005).

We are interested in the upper sign, *i.e.* the weakly absorbed wave. For this wave we obtain the following trajectory equation for small $\eta \ll 1$,

$$x_d = \frac{S_B}{2\gamma_0}(t_0 - t)\eta, \qquad t_0 = \frac{2|\chi_{rh}|\gamma_0}{S_B^2}L_0. \qquad (20)$$

As follows from (20), the coordinate x_d decreases with increasing crystal thickness t. At a certain crystal thickness $t = t_0$ the coordinate x_d stays at zero for all values of η inside the region where $\eta \ll 1$. At this thickness all rays go to the same point, which means focusing. If the crystal thickness exceeds that focusing distance $t > t_0$, then focusing takes place inside the crystal (see Fig. 8), and rays become again divergent inside the crystal, but now x_d is negative for a positive η, and *vice versa*.

Let us consider now the case $t > t_0$ and the distance L_1 behind the crystal. We obtain

$$x_d = \left[\frac{S_B}{2\gamma_0}(t_0 - t) + \frac{|\chi_{rh}|}{S_B}L_1\right]\eta. \qquad (21)$$

Here the first term in the square brackets is negative, but the second term is positive. Therefore, a second focusing is possible at a definite distance behind the crystal (see Fig. 8).

References

Afanas'ev, A. M. & Kohn, V. G. (1971). *Acta Cryst.* A**27**, 421–430.
Afanas'ev, A. M. & Kon, V. G. (1977). *Sov. Phys. Solid State*, **19**, 1035–1040.
Altarelli, M. *et al.* (2006). *The Technical Design Report of the European XFEL*, http://xfel.desy.de/technical_information/tdr/tdr/.
Aristov, V. V., Kohn, V. G., Polovinkina, V. I. & Snigirev, A. A. (1982). *Phys. Status Solidi A*, **72**, 483–491.
Aristov, V. V., Polovinkina, V. I., Afanas'ev, A. M. & Kohn, V. G. (1980). *Acta Cryst.* A**36**, 1002–1013.
Aristov, V. V., Polovinkina, V. I., Shmytko, I. M. & Shuvalov, E. V. (1978). *JETP Lett.* **28**, 4–7.
Authier, A. (2005). *Dynamical Theory of X-ray Diffraction*, 3rd ed. Oxford University Press.
Berry, M. V. & Klein, S. (1996). *Proc. Natl Acad. Sci. USA*, **93**, 2614.
Born, M. & Wolf, E. (2000). *Principles of Optics*, 7th ed. Cambridge University Press.
Dickinson, B., Seidler, G. T., Webb, Z. W., Bradley, J. A., Nagle, K. P., Heald, S. M., Gordon, R. A. & Chou, I. M. (2008). *Rev. Sci. Instrum.* **79**, 123112.
Emma, P. *et al.* (2010). *Nat. Photon.* **4**, 641–647.
Inubushi, Y., Tono, K., Togashi, T., Sato, T., Hatsui, T., Kameshima, T., Togawa, K., Hara, T., Tanaka, T., Tanaka, H., Ishikawa, T. & Yabashi, M. (2012). *Phys. Rev. Lett.* **109**, 144801.
Ishikawa, T. *et al.* (2012). *Nat. Photon.* **6**, 540–544.
Kato, N. (1961). *Acta Cryst.* **14**, 526–532.
Kleimenov, E., Bergamaschi, A., van Bokhoven, J., Janousch, M., Schmitt, B. & Nachtegaal, M. (2009). *J. Phys. Conf. Ser.* **190**, 012035.
Kohn, V. G. (1979). *Kristallografia*, **24**, 712–719. (In Russian.)
Kohn, V. G. (2012). *J. Synchrotron Rad.* **19**, 84–92.
Kohn, V. G., Snigireva, I. & Snigirev, A. (2000). *Phys. Status Solidi B*, **222**, 407–423.
Koz'mik, V. D. & Mikhailyuk, I. P. (1978). *JETP Lett.* **28**, 626–627.
Mocella, V., Ferrero, C., Hrdý, J., Wright, J., Pascarelli, S. & Hoszowska, J. (2008). *J. Appl. Cryst.* **41**, 695–700.
Mocella, V., Guigay, J. P., Hrdý, J., Ferrero, C. & Hoszowska, J. (2004). *J. Appl. Cryst.* **37**, 941–946.
Nesterets, Y. I. & Wilkins, S. W. (2008). *J. Appl. Cryst.* **41**, 237–248.
Pendry, J. B. (2000). *Phys. Rev. Lett.* **85**, 3966.
Pfeifer, T., Jiang, Y., Dusterer, S., Moshammer, R. & Ullrich, J. (2010). *Opt. Lett.* **35**, 3441–3443.
Snigirev, A., Kohn, V., Snigireva, I. & Lengeler, B. (1996). *Nature (London)*, **384**, 49–51.
Snigirev, A., Kohn, V., Snigireva, I., Souvorov, A. & Lengeler, B. (1998). *Appl. Opt.* **37**, 653–662.
Zhu, D., Cammarata, M., Feldkamp, J. M., Fritz, D. M., Hastings, J. B., Lee, S., Lemke, H. T., Robert, A., Turner, J. L. & Fenga, Y. (2012). *Appl. Phys. Lett.* **101**, 034103.